



# Sustainable treatment of harmful dyeing industry pollutants using SrZnTiO<sub>3</sub>/g-C<sub>3</sub>N<sub>4</sub> heterostructure with a light source-dependent charge transfer mechanism

Dong Jin Kim, Wan-Kuen Jo\*

Department of Environmental Engineering, Kyungpook National University, Daegu, 702–701, Republic of Korea

## ARTICLE INFO

### Keywords:

Photocatalytic dye removal  
Photostability  
Z-scheme mechanism  
Band energy structure  
Active species

## ABSTRACT

Herein, we build on the results of previous works describing the use of advanced photocatalytic processes for effective industrial wastewater treatment and investigate SrZnTiO<sub>3</sub>/g-C<sub>3</sub>N<sub>4</sub> heterostructure (SZTO/CN)-catalyzed removal of rhodamine B (RhB) and indigo carmine (IC), probing the effects of the light source (UV and visible) on charge transfer (Z-scheme and non-Z-scheme) in the above heterostructure. Both RhB (cationic dye) and IC (anionic dye) could be efficiently removed by SZTO/CN, which also exhibited elevated photocurrent responses. In particular, the efficiencies of IC and RhB removal over a SZTO/CN sample with a CN/(SZTO + CN) mass ratio of 0.8 after 3-h visible-light irradiation equaled 93.1 and 82.2%, respectively, while the respective values for STO were obtained as 9.7 and 21.8%. Dye degradation under UV light irradiation (e.g., within 30 min for IC) was much faster than under visible light irradiation (e.g., within 180 min for IC), and optimal CN/(SZTO + CN) ratios were individually determined for both irradiation types. Notably, the best performing catalyst maintained over 95% of its initial photocatalytic performance after five consecutive IC decomposition runs, and the X-ray diffraction patterns of cycled and non-cycled catalysts indicated that cycling did not induce any notable crystalline structure changes. The reactive species involved in photocatalytic degradation were identified as O<sub>2</sub><sup>•−</sup>, h<sup>+</sup>, and OH<sup>•</sup> for both light source types, which, together with the results of band energy structure analysis and hydroxyl radical population measurements allowed us to propose two light source-dependent photocatalytic dye removal mechanisms. Thus, it was concluded that the developed SZTO/CN heterostructure can be sustainably applied to the treatment of dye-contaminated wastewater.

## 1. Introduction

Use of (synthetic) dyes in the textile industry inevitably results in the discharge of dye-contaminated wastewater and thus causes environmental pollution [1]. For example, the inefficiency of dying processes results in a release of 10–50% of colorants into the environment [2], which can inflict serious damage to aquatic ecosystems and reduce the aesthetic appeal of receiving water bodies [3–5]. Therefore, in order for the textile dyeing industry to be sustainable, dye-containing effluents should be efficiently treated (e.g., using advanced photocatalytic processes [6,7]) prior to discharge.

Use of heterogeneous photocatalysts such as metal oxide semiconductors for the treatment of contaminated wastewater has recently attracted much attention [8–13]. In particular, perovskite strontium titanate (SrTiO<sub>3</sub> (STO), bandgap = 3.10–3.22 eV) is an attractive p-type semiconductor photocatalyst exhibiting the advantages of high

photochemical stability, natural abundance, and excellent catalytic activity [14–19]. In addition, STO features a conduction band (CB) edge that is 200 mV more negative than that of pure TiO<sub>2</sub> and therefore exhibits a photocatalytic reduction potential superior to that of the latter [15,17]. Nevertheless, the stand-alone use of STO is restricted by the high rate of charge carrier recombination and the resulting low quantum efficiency [15–19], which necessitates the above catalyst to be modified for better performance. For example, doping of STO with metals such as Zn, Cr, and La can enhance its photocatalytic performance for pollutant removal or hydrogen generation [14,15]. Specifically, metals doped semiconductors can extend light absorption into the visible region to enhance the photocatalytic efficiency of the semiconductors [14,15].

The combination of a broad-bandgap semiconductor with a narrow-bandgap semiconductor to produce a heterostructure results in optical property and charge separation efficiency improvements and is

\* Corresponding author.

E-mail address: [wkjo@knu.ac.kr](mailto:wkjo@knu.ac.kr) (W.-K. Jo).

<https://doi.org/10.1016/j.apcatb.2018.10.001>

Received 9 July 2018; Received in revised form 26 September 2018; Accepted 1 October 2018

Available online 04 October 2018

0926-3373/ © 2018 Elsevier B.V. All rights reserved.

therefore a viable technique of photocatalytic performance enhancement [20,21]. Graphitic carbon nitride (g-C<sub>3</sub>N<sub>4</sub>, CN) features a narrow bandgap of ~2.7 eV and conduction and valence band (VB) edges of -1.1 and +1.6 eV, respectively, additionally exhibiting the advantages of high chemical/thermal stability and excellent visible light absorption efficiency [22,23]. In addition, the two-dimensional (2D) structure of CN can be easily incorporated into zero-dimensional (0D) particles to establish 0D/2D heterostructures with enhanced photocatalytic activity [22]. Similarly, it is suggested that 0D metal-impregnated STO/2D CN heterostructures should be easy to fabricate and be well suited for the photocatalytic removal of dyes.

Two types of semiconductor-semiconductor heterostructures (staggered arrangement type II heterojunctions and Z-scheme systems) have been developed for environmental pollutant treatment [24]. The former systems achieve effective spatial separation of charge carriers by making use of the band potential arrangement between two semiconductors but exhibit low redox capability caused by the movement of photogenerated electrons and holes to lower reduction and oxidation potentials, respectively [24]. This handicap can be overcome by the use of Z-scheme systems, which replicate the natural process of photosynthesis in green plants, since the redox capabilities of photogenerated electrons and holes in these systems exceed those of type II heterostructures [24]. Therefore, the development of Z-scheme systems is preferred to that of type II heterojunctions.

Herein, we explore the photocatalytic dye removal performance of a novel low-cost metal (Zn)-impregnated SrTiO<sub>3</sub>/g-C<sub>3</sub>N<sub>4</sub> heterostructure (SZTO/CN). In particular, since this heterostructure comprises both UV light- (SZTO) and visible light-activated (CN) components, two light sources (UV and visible light lamps) were utilized to understand light source-dependent charge transfer processes. Two commonly employed rhodamine B (RhB) and indigo carmine (IC) dyes were selected as model pollutants based on their prevalence in wastewaters from textile and other industries and their toxic effects [3,25]. For comparison, the photocatalytic degradation of these dyes was also investigated for STO, SZTO, and CN as reference catalysts, and the photostability of SZTO/CN was characterized in detail. Finally, valuable mechanistic insights into SZTO/CN-catalyzed dye removal were obtained by performing active species tests, band energy structure analysis, and hydroxyl radical population measurements, which allowed two distinct light source-dependent degradation mechanisms to be proposed.

## 2. Experimental

### 2.1. Photocatalyst preparation

SZTO was prepared using the polymeric citrate precursor method. Ti(IV) isopropoxide (97.0%; 4.0 mL) was added to anhydrous ethylene glycol (99.8%; 30 mL), and the mixture was stirred for 1 h, sequentially treated with citric acid (99.5%; 25.5 g) and [Sr(NO<sub>3</sub>)<sub>2</sub> (99.0%; 2.7 g) + Zn(NO<sub>3</sub>)<sub>2</sub>·6H<sub>2</sub>O (0.2 g)] upon stirring, and further stirred for 1 h to afford SZTO (Sr<sub>0.95</sub>Zn<sub>0.05</sub>TiO<sub>3</sub>). Subsequent heating in an oil bath (120 °C, 9 h) afforded a brown paste that was annealed at 400 °C for 2 h, ground into a fine powder, and heated in a tube furnace at 800 °C for 5 h to afford SZTO powder. In addition, an STO sample was prepared using the same procedure in the absence of Zn(NO<sub>3</sub>)<sub>2</sub>·6H<sub>2</sub>O.

SZTO/CN was fabricated by hybridizing SZTO with CN. To prepare bulk CN, ground melamine (5 g) was transferred to an alumina boat, calcined at 500 °C for 0.5 h and then at 550 °C for 3 h, and cooled. Sheet CN (0.5 g), prepared by calcining bulk CN at 500 °C for 2 h, cooling, and grinding, and a specified amount of SZTO powder were dispersed in methanol (20 mL), and the dispersion was stirred for 24 h, dried at 80 °C for 12 h, and annealed at 500 °C for 2 h to afford SZTO/CN powder. SZTO/CN samples with CN/(SZTO + CN) mass ratios of 0.5, 0.6, 0.7, and 0.8 (SZTO/CN-0.5, SZTO/CN-0.6, SZTO/CN-0.7, and SZTO/CN-0.8, respectively) were prepared using SZTO amounts of 0.50, 0.33, 0.21, and 0.13 g, respectively.

The synthesized catalysts were examined by X-ray diffraction spectroscopy (XRD), high-resolution field-emission transmission electron microscopy (HRTEM) coupled with energy-dispersive X-ray spectroscopy (EDX), UV-vis (UV-vis) spectroscopy, X-ray photoelectron spectroscopy (XPS), photoluminescence (PL) spectroscopy, and Fourier transform infrared (FTIR) spectroscopy. Detailed information on analytical instruments is provided in the Supplementary Material.

### 2.2. Photocatalytic degradation experiments

The efficiencies of aqueous-phase IC and RhB degradation over the synthesized samples were assessed under illumination with visible (500-W halogen lamp equipped with an optical cut-off filter ( $\lambda > 420$  nm) or UV (400-W high-pressure mercury lamp) light using a Pyrex® reaction unit cooled by water circulating through outer Tygon® tubing to minimize the effect of irradiation-induced heating. The chemical structures of IC and RhB were provided in Fig. S1. A photolysis experiment was performed in the absence of photocatalysts, and photocatalyst adsorption tests were performed in the absence of light. For photocatalytic degradation tests, each photocatalyst (20 mg) was suspended in IC (20 mg L<sup>-1</sup>), RhB (5 mg L<sup>-1</sup>), or isoniazid (5 mg L<sup>-1</sup>) solutions (200 mL), and the obtained suspensions were vigorously stirred for 0.5 h prior to illumination to establish an adsorption equilibrium. Isoniazid was selected as a model non-dye pollutant to compare its photocatalytic degradation efficiency with those of IC and RhB under visible light illumination. Water probes sampled at a specified time interval were filtered through a 0.2- $\mu$ m PTFE filter (Advantec Co.) to remove residual photocatalyst particles, and the filtrates were analyzed using a UV-vis spectrometer (Shimadzu UV-2600) at the wavelength of maximal absorption for each pollutant. Additionally, five cycling tests were carried out to investigate the photostability of a representative SZTO/CN sample (SZTO/CN-0.8). Total organic carbon (TOC) measurements were also performed using a Portable TOC Analyzer 820 to verify the mineralization ability of the representative SZTO/CN catalyst (SZTO/CN-0.8). High performance liquid chromatography/tandem mass spectrometry (LC/MS/MS, Dionex Ultimate 3000 and Thermo Scientific TSQ Quantiva) was employed to examine the formation of byproducts.

### 2.3. Photocurrent measurements

Photocurrent measurements for CN, STO, SZTO, STO/CN, and SZTO/CN-0.8 samples were performed using an electrochemical analyzer (Oriol Instruments Model 66902) with three electrode units. The working electrode was prepared by heating catalyst-coated indium tin oxide at 300 °C for 2.5 h. The working, reference, and counter electrodes were operated in an electrolyte solution (Na<sub>2</sub>SO<sub>4</sub>, 0.5 M) upon stirring, and photocurrent responses were recorded upon illumination with a 300-W xenon lamp equipped with a visible-light or UV cutoff filter.

### 2.4. Active species tests

Detailed methods for the above test are described in the Supplementary Material.

## 3. Results and discussion

### 3.1. Material properties

Fig. 1 presents the XRD spectra of STO, CN, SZTO, and SZTO/CN-0.8, showing that the pattern of non-modified STO, SZTO, and SZTO/CN-0.8 featured distinct peaks at  $2\theta = 22.70^\circ$ ,  $32.32^\circ$ ,  $39.90^\circ$ ,  $46.40^\circ$ ,  $52.30^\circ$ ,  $57.70^\circ$ ,  $67.74^\circ$ ,  $72.48^\circ$ ,  $77.12^\circ$ ,  $81.60^\circ$ , and  $86.14^\circ$ , which were indexed to the (100), (110), (111), (200), (210), (211), (220), (300), (310), (311), and (222) planes of STO, respectively, in accordance with

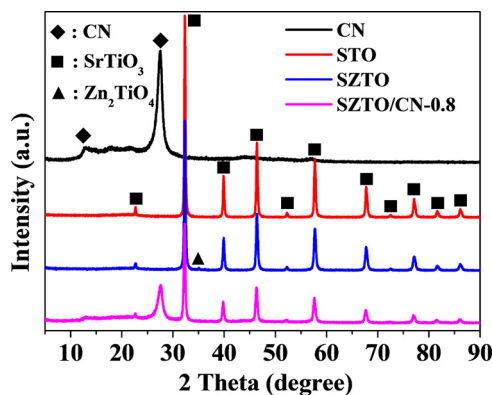


Fig. 1. XRD patterns of CN, STO, SZTO, and SZTO/CN-0.8.

the standard data for cubic STO (JCPDS No. 01-070-8508). In addition, the XRD pattern of SZTO displayed a peak at  $35.07^\circ$ , which corresponded to the (311) plane of  $\text{Zn}_2\text{TiO}_4$  (JCPDS No. 01-073-0578). Although this peak was hardly observed for SZTO/CN-0.8, probably in view of the low (below the detection level) amount of Zn therein, the presence of Zn in SZTO/CN-0.8 was confirmed by HRTEM mapping/EDX images (Fig. 2), which also revealed the presence of Sr, Ti, O, N, and C. Similarly to that of pure CN, the diffractogram of SZTO/CN-0.8 contained two CN-associated peaks at  $12.94^\circ$  and  $27.46^\circ$ , which were indexed to the (100) and (002) planes of CN, respectively (JCPDS No. 87-1526). In addition, TEM and HRTEM images of SZTO/CN-0.8 illustrated that SZTO nanoparticles were well distributed on the 2D CN sheets (Fig. 3).

Figs. S1 and S2 illustrate the chemical composition and elemental states of SZTO-0.8, respectively. The full-scan XPS spectrum of SZTO-0.8 featured peaks of Sr, Ti, O, Zn, C, and N (Fig. S2), and the corresponding Sr 3d spectrum (Fig. S3a) contained Sr  $3d_{5/2}$  and Sr  $3d_{3/2}$  peaks at 133.4 and 135.3 eV, respectively [18,26]. The Ti 2p peaks at 458.8 and 464.2 eV in Fig. S3b were ascribed to Ti  $2p_{3/2}$  and Ti  $2p_{1/2}$  transitions, respectively, while O 1s peaks at 530.1 and 532.6 eV in Fig. S3c were ascribed to Ti–O bonds and oxygen vacancies, respectively [27]. The Zn 2p spectrum of SZTO-0.8 (Fig. S3d) featured distinct peaks at 1021.1 (Zn  $2p_{3/2}$ ) and 1045.1 eV (Zn  $2p_{1/2}$ ) [28,29]. Fig. S3e shows the corresponding C 1s spectrum, with the peak at 288.2 eV ascribed to N–C=N moieties in CN, while that at 284.9 eV was associated with adventitious carbon [30]. The N 1s spectrum of SZTO-0.8 (Fig. S3f)

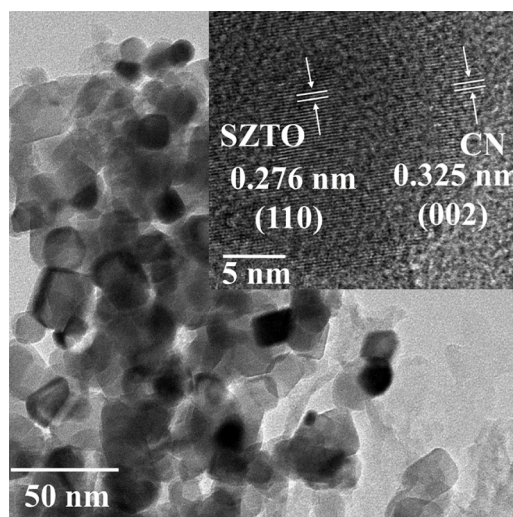


Fig. 3. TEM and HRTEM (inset) images of SZTO/CN-0.8.

featured peaks at 398.6, 400.5, 401.7, and 404.3 eV, which were attributed to C–N=C, N–(C)<sub>3</sub>, C–N–H, and  $\pi$  excitations, respectively [30].

The bonding structures of CN, STO, SZTO, and SZTO/CN-0.8 were examined by FTIR spectroscopy (Fig. S4). For pure CN, the peak at  $804\text{ cm}^{-1}$  was ascribed to s-triazine unit vibrations, while peaks between  $1202$  and  $1629\text{ cm}^{-1}$  and between  $2922$  and  $3369\text{ cm}^{-1}$  were attributed to general C–N stretching and amino group N–H stretching vibrations, respectively [31,32]. For both STO and SZTO samples, the peaks at  $448$  and  $532\text{ cm}^{-1}$  were ascribed to vibrations of Ti–O and Sr–O bonds, respectively [33], whereas the peak at  $439\text{ cm}^{-1}$  observed for SZTO was attributed to ZnO stretching [34]. Finally, both SZTO- and CN-associated peaks were detected for SZTO/CN-0.8, which was indicative of an interconnection between SZTO particles and CN sheets.

Fig. 4 presents the UV–vis absorption spectra of CN, STO, SZTO, and SZTO/CN-0.8, demonstrating that STO exhibited strong absorption in the UV range and featured a bandgap of 3.19 eV, in agreement with previously reported values [18,35]. The maximum absorption wavelength of SZTO was only slightly red-shifted (bandgap = 3.17 eV) compared to that of STO, whereas significant red shifts were observed for both CN and SZTO/CN-0.8 (bandgaps = 2.67 and 2.79 eV, respectively). Thus, the above findings indicated that SZTO catalysts could be

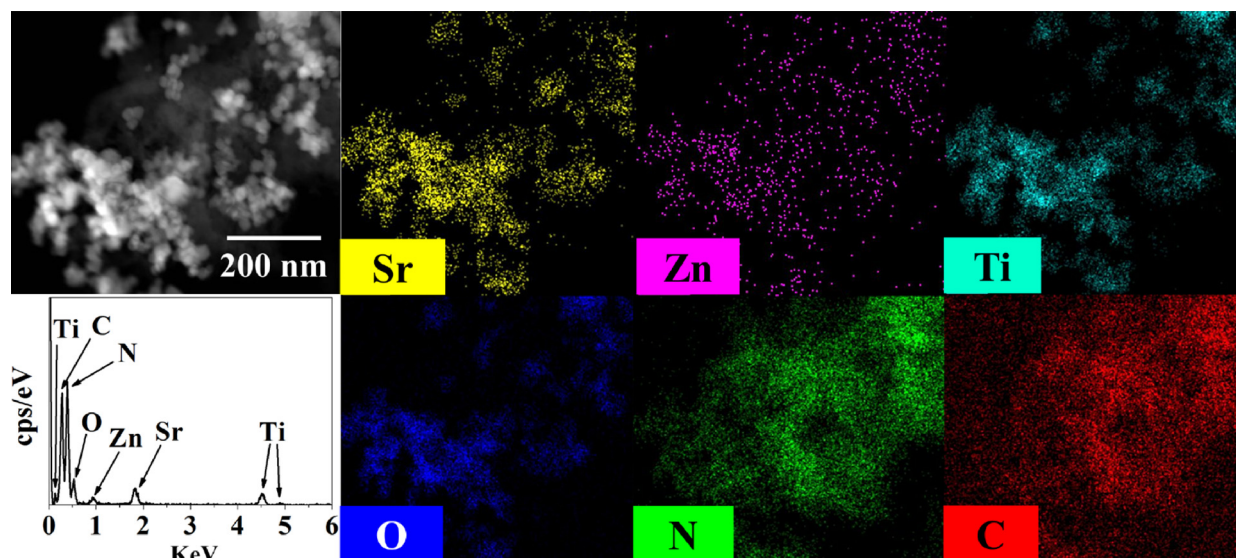


Fig. 2. HRTEM mapping/EDX images of SZTO/CN-0.8.

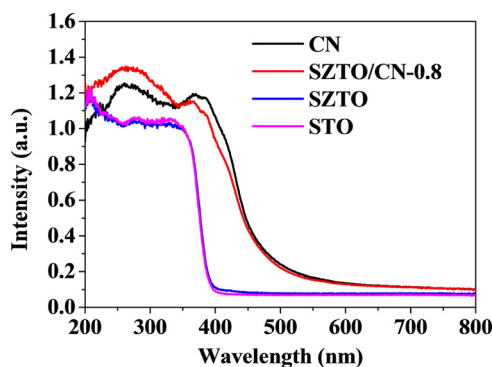


Fig. 4. UV-vis absorption spectra of CN, STO, SZTO, and SZTO/CN-0.8.

activated by visible light irradiation. Fig. S5 displays the bandgaps of samples, which were determined based on the plot of transformed Kubelka-Munk function versus the energy of light.

### 3.2. Photocatalytic dye degradation

The efficiencies of photocatalytic IC and RhB removal were evaluated using a cylindrical Pyrex<sup>®</sup> reaction unit. The adsorption efficiencies of the photocatalysts for the target pollutants, which were determined in the dark, were much lower ( $< 1.5\%$  for IC and  $< 3.5\%$  for RhB) than the respective photocatalytic degradation efficiencies. No significant dye degradation was observed in the absence of catalysts, whereas extensive decomposition was observed upon visible light irradiation in the presence of STO, SZTO, CN, and SZTO/CN (Fig. 5). The obtained removal efficiencies increased in the order of: STO, SZTO  $<$  CN  $<$  SZTO/CN-0.8, which matched the order of photocurrent responses (Fig. S6). Moreover, the order of removal efficiencies matched that of the kinetic rate constants, which were determined using the kinetic plot for the photocatalytic decomposition of IC and RhB over STO, SZTO, CN, and SZTO/CN-0.8 under visible light illumination (Fig. S7); the rate constants of STO, SZTO, CN, and SZTO/CN-0.8 for IC degradation were  $\sim 0$ ,  $\sim 0$ ,  $0.00333$ , and  $0.0117 \text{ min}^{-1}$ , respectively, while the respective values for RhB degradation were  $\sim 0$ ,  $\sim 0$ ,  $0.00258$ , and  $0.00827 \text{ min}^{-1}$ .

The kinetic rate constants and test conditions for IC and RhB degradation obtained from this and other studies are shown in Table S1. The rate constants were normalized to catalyst dosage avoid the potential effect of sample amount. The normalized rate constants found in the present study for IC ( $0.117 \text{ min}^{-1}/(\text{g L}^{-1})$ ) and RhB ( $0.0827 \text{ min}^{-1}/(\text{g L}^{-1})$ ) were higher than the corresponding rate constants reported in previous studies, which suggested the improved activity of SZTO/CN-0.8 fabricated herein. Nevertheless, it is noteworthy that rate constants may not scale linearly with sample amount. Moreover, other test conditions such as initial concentration, reactor shape, lamp type, and light transmittance might have induced variability in rate constants.

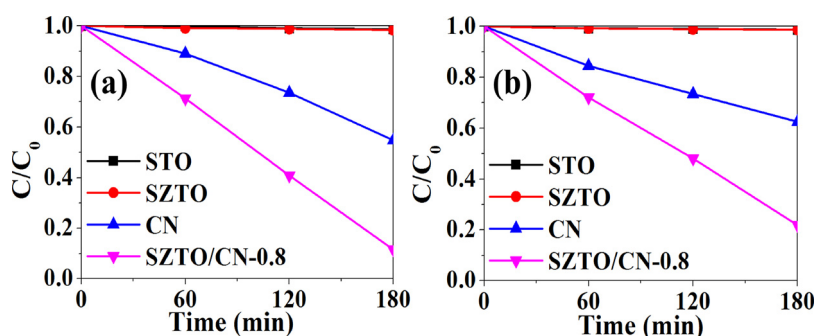


Fig. 5. Efficiencies of (a) IC and (b) RhB removal by CN, STO, SZTO, and SZTO/CN-0.8 under visible light irradiation.  $C_0$  and  $C$  represent pollutant concentrations before and after irradiation, respectively.

In particular, the efficiencies of IC and RhB removal over SZTO/CN-0.8 after 3-h visible-light irradiation equaled 88.4 and 78.1%, respectively, while the respective values for STO were obtained as  $\sim 0\%$  (Fig. 5). The superior photocatalytic performance of the SZTO/CN hybrid was ascribed to the movement of photoexcited electrons from the CB of CN to that of STO, which increased the charge separation efficiency and thus enhanced photocatalytic performance, as described in detail in Section 3.4. Although the visible light absorption efficiency of SZTO/CN-0.8 was lower than that of CN (but exceeded those of STO and SZTO), the former catalyst achieved a higher dye removal efficiency than the latter, which implied that this parameter is largely determined by charge separation efficiency and not by visible light absorption efficiency. This assertion is supported by the PL emission analyses of the photocatalysts (Fig. S8): the PL emission intensity of SZTO/CN-0.8 was lower than those of CN and STO/CN, indicating that SZTO/CN-0.8 exhibited higher charge separation efficiency.

Fig. 6 shows the efficiencies of UV illumination-driven dye removal for STO, SZTO, CN, and SZTO/CN, demonstrating that although these efficiencies followed the same order as that observed for visible light illumination, the overall degradation rate was much faster in the former case. Additionally, as observed for visible light illumination, the order of UV illumination-driven dye removal efficiencies matched that of the corresponding photocurrent responses (Fig. S9). The superior photocatalytic performance of SZTO/CN under UV light irradiation was mainly assigned to the operation of the Z-scheme reaction process (described in detail in Section 3.4.), which resulted in improved charge separation efficiency and thus enhanced the photocatalytic activity.

Subsequently, we examined the effect of the CN/(SZTO + CN) ratio on pollutant removal efficiency. Fig. 7 reveals the efficiencies of IC removal by SZTO/CN samples with different CN/(SZTO + CN) ratios under visible light irradiation, demonstrating that this efficiency increased as the above ratio was increased from 0.6 to 0.8 and decreased as this ratio was further increased to 0.9, in agreement with the pattern of photocurrent responses obtained for visible light (Fig. S10). Therefore, the CN/(SZTO + CN) ratio of 0.8 (SZTO/CN-0.8) was concluded to be best suited for IC removal. Fig. S11 reveals the efficiencies of IC removal by SZTO/CN samples with different CN/(SZTO + CN) ratios under UV light irradiation, showing that the removal efficiency increased as the above ratio was increased from 0.6 to 0.7 and then decreased upon a further increase of this ratio, in agreement with the behavior observed for the corresponding photocurrent responses (Fig. S12).

TOC analysis was performed during the degradation of IC and RhB by SZTO/CN-0.8 to assess the mineralization abilities of these contaminants under visible light irradiation. TOC removal abilities of IC and RhB after 3-h illumination reached 52.2 and 38.7%, respectively (Fig. S13). These TOC removal abilities of IC and RhB were lower than the respective degradation abilities (88.4 and 78.1%, respectively) (Fig. 5), indicating the formation of byproducts. The intermediates/byproducts generated during the photocatalytic decomposition of RhB

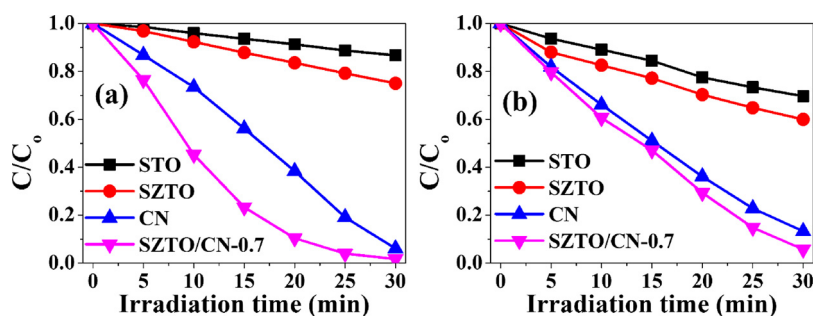


Fig. 6. Efficiencies of (a) IC and (b) RhB removal by CN, STO, SZTO, and SZTO/CN-0.8 under UV light irradiation.

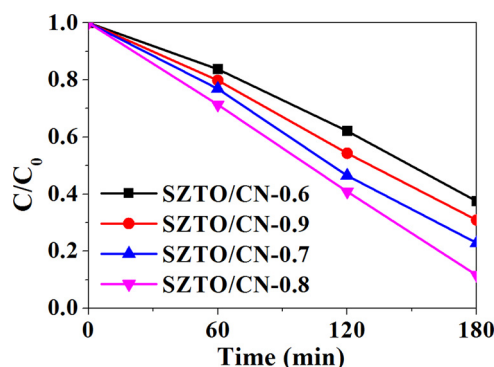


Fig. 7. Efficiencies of IC removal by SZTO/CN samples with different CN/(SZTO + CN) ratios under visible light irradiation.

and IC were determined by the LC/MS/MS analyses. Fig. S14 displays the LC/MS/MS spectra of samples taken after 3-h degradation of RhB and IC. The peak observed at an  $m/z$  value of 443.29 corresponded to the pristine RhB (Fig. S14a-1), while the peaks of 415.25, 387.45, 359.36, and 331.28 were associated with N-deethylated intermediary compounds (Figs. S14a-1 to S14a-4) [35–37]. RhB could further be decomposed to the end products with the  $m/z$  values of 147.88, 138.52, 132.55, 118.22, 104.11, and 90.51, which were assigned to adipic acid, 3-hydroxybenzoic acid, pentanedioic acid, succinic acid, malonic acid, and oxalic acid, respectively (Fig. S14a-5) [35–37]. Additionally, the peak observed at an  $m/z$  value of 209.18 corresponded to the pristine IC, while the peaks of 226.03 and 244.06 were ascribed to the C=C bond breaking of IC and isatin sulfonic acid, respectively (Fig. S14b) [38]. Nevertheless, the peak areas of byproducts in the spectra were much lower than those of pristine RhB and IC, suggesting that health risk from exposure to the byproducts is not significant.

### 3.3. Photostability

The photostability of a given catalyst is a crucial factor determining its practical applicability to pollutant removal [18,39]. Herein, the photostability of SZTO/CN-0.8 was evaluated by subjecting it to five successive runs of UV light-driven IC removal. As shown in Fig. 8, the SZTO/CN sample maintained over 95% of its initial photocatalytic activity after the final run, and this slight decrease of photocatalytic decomposition activity was ascribed to inevitable catalyst loss during cycling. In addition, the XRD patterns of pristine and spent SZTO/CN-0.8 indicated that cycling did not result in notable crystalline structure changes (Fig. S15). Accordingly, the fabricated SZTO/CN hybrid was concluded to exhibit high photostability and therefore be a competitive candidate for long-term practical utilization in water pollutant treatment.

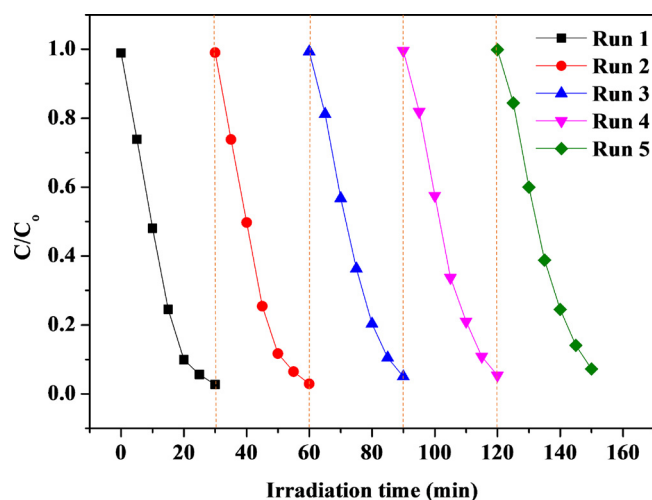


Fig. 8. Results of SZTO/CN-0.8 photostability testing (five cycles of photocatalytic IC degradation under UV light irradiation).

### 3.4. Band energy diagram and photocatalytic reaction mechanism

The band energy diagrams of CN and SZTO in SZTO/CN photocatalysts are displayed in Fig. 9. The bandgap (2.7 eV) and VB (+1.64 eV) energies of CN were obtained from its UV–vis absorption (Fig. 4) and VB XPS (Fig. S16) spectra, respectively, with the corresponding values of SZTO determined as 3.2 and +2.83 eV, respectively. Fig. 9 also illustrates a plausible mechanism of SZTO/CN-catalyzed dye removal, suggesting that illumination with visible light excites the VB electrons of CN to its CB and concomitantly generates  $h^+$  in its VB, whereas neither electron excitation nor  $h^+$  generation occurs for SZTO owing to its large bandgap (3.2 eV) (Fig. 9a). Further migration of excited electrons to the CB of SZTO, which exhibits a less negative potential than the CB of CN, enhances the efficiency of  $e^-h^+$  pair separation. Additionally, dye materials might absorb visible light to excite electrons, which could migrate to the CB of SZTO or CN, facilitating the degradation of dye molecules [41]. Since the CB potential of SZTO is more negative than the  $O_2/O_2^{\cdot-}$  reduction potential (−0.33 eV vs. NHE) [40], the migrated  $e^-$  react with oxygen to form  $O_2^{\cdot-}$  (superoxide) radicals that degrade organic pollutants to produce  $CO_2$  and other intermediates. Superoxide radicals can react with  $H_2O$  to generate hydroxyl radicals ( $OH^{\cdot}$ ), which, together with  $h^+$  remaining in the VB of CN, also contribute to pollutant degradation [42]. To confirm/disprove the suggested mechanism, we investigated the contribution of active species to the photocatalytic removal process by performing degradation experiments in the presence of various scavengers under visible light. Fig. 10a demonstrates that all three active species (i.e.,  $O_2^{\cdot-}$ ,  $h^+$ , and  $OH^{\cdot}$ ) played important roles in the photocatalytic removal of IC, with the highest contribution observed for  $O_2^{\cdot-}$ . In addition, photocatalytic degradation was also shown to involve the formation of  $OH^{\cdot}$  (Fig. 11a). It is noteworthy that the photocatalytic degradation

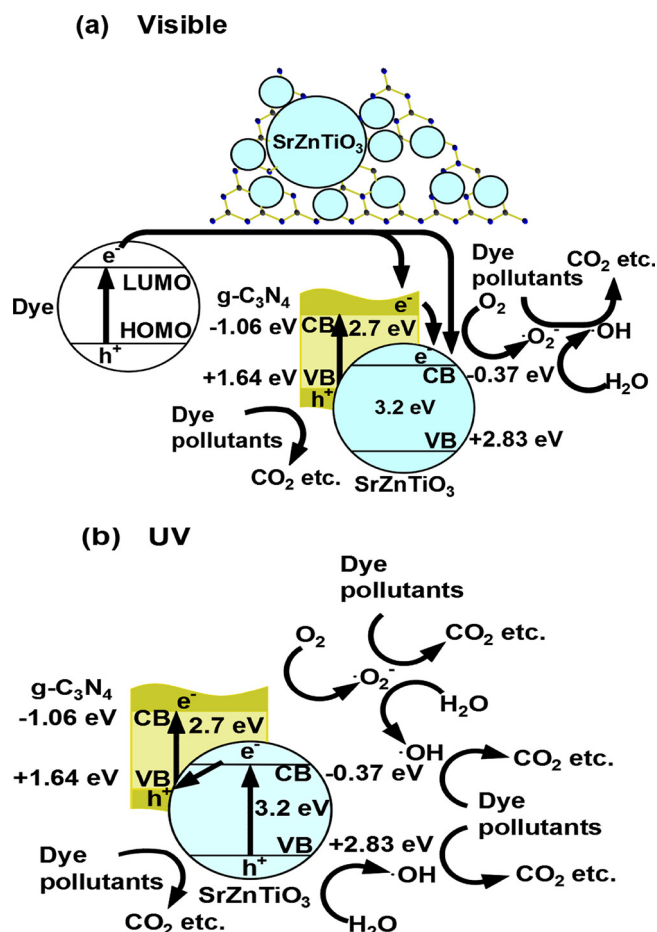


Fig. 9. Schematic band energy diagrams of CN and SZTO in SZTO/CN and the mechanism of photocatalytic dye removal by SZTO/CN under (a) visible light and (b) UV light irradiation.

efficiencies of IC (88.4%) and RhB (78.1%) after 3-h visible light illumination were higher than that of a non-dye pollutant, isoniazid (48.5%) (Fig. S17), possibly owing to the photosensitization of dye molecules.

In contrast to the case of visible light illumination, UV illumination was suggested to result in electron excitation and  $h^+$  generation in both CN and SZTO (Fig. 9b). In this case, the migration of excited electrons from the CB of SZTO to the VB of CN and their combination with photogenerated holes results in the accumulation of holes and electrons in the VB of SZTO and the CB of CN, respectively, which corresponds to a Z-scheme charge transfer process. Therefore, Z-scheme SZTO/CN photocatalysts should exhibit a strong redox capacity, since the reduction potential of  $e^-$  in the CB of CN exceeds that of  $e^-$  in the CB of SZTO, while the oxidation potential of  $h^+$  in SZTO exceeds that of  $h^+$  in

CN. The holes in the VB of SZTO can react with  $OH^-$  to afford  $OH^\cdot$ , since the VB potential (+2.83 eV) of SZTO is more positive than the  $OH^-/OH^\cdot$  oxidation potential (+2.38 eV vs. NHE) [40]. Moreover, electrons in the CB of CN can convert  $O_2$  to  $O_2^{\cdot-}$ , since the CB potential (-1.06 eV) of CN is more negative than the  $O_2/O_2^{\cdot-}$  reduction potential (-0.33 eV vs. NHE) [40]. Similarly to the case of visible light illumination, the reactive species test performed under UV light illumination showed that  $O_2^{\cdot-}$ ,  $h^+$ , and  $OH^\cdot$  were all actively involved in the photocatalytic removal of IC, with the highest contribution observed for  $O_2^{\cdot-}$  (Fig. 10b). Notably, more hydroxyl radicals were generated under UV light illumination than under visible light illumination (Fig. 11a and b), which was ascribed to the fact that these radicals were most likely produced by the reaction of  $h^+$  in the VB of SZTO with  $OH^-$  under UV light irradiation. Consequently, the fact that the photocatalytic performance of SZTO/CN was higher under UV light irradiation was ascribed to the operation of a Z-scheme mechanism under these conditions.

#### 4. Conclusions

Herein, we explored the photocatalytic dye removal performance of a novel low-cost metal (Zn)-impregnated  $SrTiO_3/g-C_3N_4$  heterostructure. In particular, since this heterostructure comprises both UV light- (SZTO) and visible light-activated (CN) components, two light sources (UV and visible light lamps) were utilized to understand light source-dependent charge transfer processes. We showed that large-bandgap 0D Zn-impregnated  $SrTiO_3$  can be easily hybridized with narrow-bandgap 2D  $g-C_3N_4$  to afford an SZTO/CN heterostructure exhibiting an improved photocatalytic dye degradation performance and featuring light source-dependent charge transfer processes. Moreover, SZTO/CN exhibited high photostability and photocurrent responses, which was assigned to enhanced charge separation efficiency, and featured CN/(SZTO + CN) ratio-dependent photocatalytic activity. The abovementioned hybrid could be operated as a Z-scheme semiconductor-semiconductor system under UV light illumination and was therefore superior to type II heterojunction photocatalysts. Upon visible light illumination, the migration of  $e^-$  from the CB of CN to the CB of SZTO increased the efficiency of charge separation, and this increase was even more pronounced upon UV irradiation in view of the concomitant Z-scheme charge movement between CN and SZTO. In view of the above, the newly developed SZTO/CN heterostructure was concluded to be suitable for sustainable degradation of both dye- and other pollutant-contaminated industrial wastewater.

#### Disclosure statement

The author declares that no conflicting actual or potential interests exist.

#### Acknowledgements

This work was supported by the National Research Foundation of

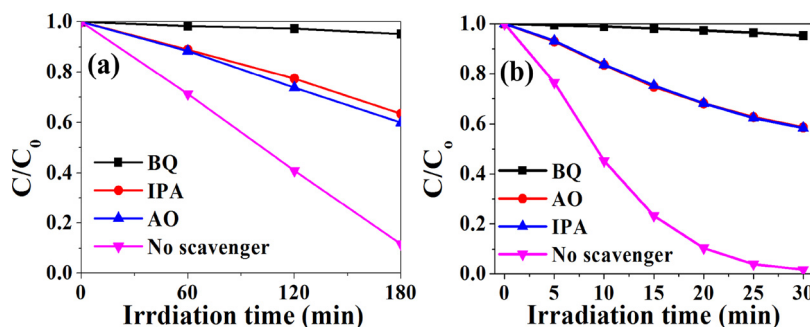


Fig. 10. Active species trapping experiments performed for IC degradation over SZTO/CN-0.8 under (a) visible light and (b) UV light irradiation.

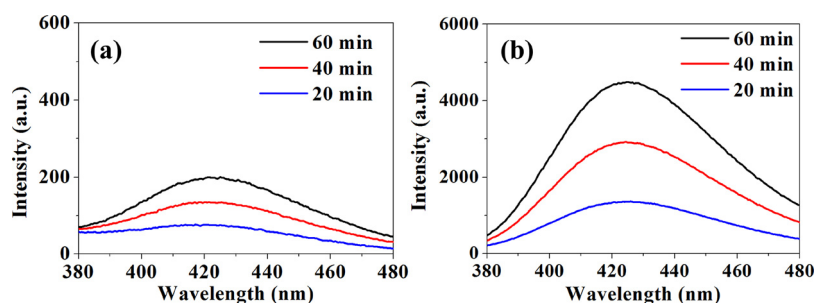


Fig. 11. Fluorescence spectra of SZTO/CN-0.8 used to determine hydroxyl radical populations for (a) visible light and (b) UV light exposures of 20, 40, and 60 min.

Korea (NRF) grant funded by the Korea government (MSIP) (No. 2016R1A2B4009122 and 2017R1A4A1015628).

## Appendix A. Supplementary data

Supplementary material related to this article can be found, in the online version, at doi:<https://doi.org/10.1016/j.apcatb.2018.10.001>.

## References

- [1] C.D. Raman, S. Kanmani, Textile dye degradation using nano zero valent iron, *J. Environ. Manage.* 177 (2016) 341–355.
- [2] W. Przysała, E. Zabłocka-Godlewska, E. Grabińska-Sota, Biological removal of azo and triphenylmethane dyes and toxicity of process by-products, *Water Air Soil Poll.* 223 (2012) 1581–1592.
- [3] I. Nath, J. Chakraborty, P.M. Heynderickx, F. Verpoort, Engineered synthesis of hierarchical porous organic polymers for visible light and natural sunlight induced rapid degradation of azo, thiazine and fluorescein based dyes in a unique mechanistic pathway, *Appl. Catal. B* 227 (2018) 102–113.
- [4] M. Sarvajith, G.K.K. Reddy, Y.V. Nancharaiiah, Textile dye biodecolorization and ammonium removal over nitrite in aerobic granular sludge sequencing batch reactors, *J. Hazard. Mater.* 342 (2018) 536–543.
- [5] X. Chen, Q. Deng, S. Lin, C. Du, S. Zhao, Y. Hu, Z. Yang, Y. Lyu, A new approach for risk assessment of aggregate dermal exposure to banned azo dyes in textiles, *J. Han Regul. Toxicol. Pharmacol.* 91 (2017) 173–178.
- [6] T.S. Natarajan, K.R. Thampi, R.J. Tayade, Visible light driven redox-mediator-free dual semiconductor photocatalytic systems for pollutant degradation and the ambiguity in applying Z-scheme concept, *Appl. Catal. B* 227 (2018) 296–311.
- [7] Z. Xing, J. Zhang, J. Cui, J. Yin, T. Zhao, J. Kuang, Z. Xiu, N. Wan, W. Zhou, Recent advances in floating TiO<sub>2</sub>-based photocatalysts for environmental application, *Appl. Catal. B* 225 (2018) 452–467.
- [8] M. May-Lozano, V. Mendoza-Escamilla, E. Rojas-García, R. López-Medina, G. Rivadeneyra-Romero, S.A. Martínez-Delgadillo, Sonophotocatalytic degradation of Orange II dye using low cost photocatalyst, *J. Clean. Prod.* 148 (2017) 836–844.
- [9] X. Zhang, Y. Wang, B. Liu, Y. Sang, H. Liu, Heterostructures construction on TiO<sub>2</sub> nanobelts: a powerful tool for building high-performance photocatalysts, *Appl. Catal. B* 202 (2017) 620–641.
- [10] X. Zhao, X. Liu, M. Yu, C. Wang, J. Li, The highly efficient and stable Cu, Co, Zn-porphyrine TiO<sub>2</sub> photocatalysts with heterojunction by using fashioned one-step method, *Dye. Pigment.* 136 (2017) 648–656.
- [11] V. Vaiano, O. Sacco, D. Sannino, P. Ciambelli, Process intensification in the removal of organic pollutants from wastewater using innovative photocatalysts obtained coupling Zinc Sulfide based phosphors with nitrogen doped semiconductors, *J. Clean. Prod.* 100 (2015) 208–211.
- [12] M. Anas, D.S. Han, K. Mahmoud, H. Park, A. Abdel-Wahab, Photocatalytic degradation of organic dye using titanium dioxide modified with metal and non-metal deposition, *Mater. Sci. Semicon. Proc.* 41 (2016) 209–218.
- [13] A. Salama, A. Mohamed, N.M. Aboamra, T.A. Osman, A. Khattab, Photocatalytic degradation of organic dyes using composite nanofibers under UV irradiation, *Appl. Nanoscience* 8 (2018) 155–161.
- [14] J.P. Zou, L.Z. Zhang, S.L. Luo, L.H. Leng, X.B. Luo, M.J. Zhang, Y. Luo, G.C. Guo, Preparation and photocatalytic activities of two new Zn-doped SrTiO<sub>3</sub> and BaTiO<sub>3</sub> photocatalysts for hydrogen production from water without cocatalysts loading, *Int. J. Hydrogen Energy* 37 (2012) 17068–17077.
- [15] S. Tonda, S. Kumar, O. Anjaneyulu, V. Shanker, Synthesis of Cr and La-codoped SrTiO<sub>3</sub> nanoparticles for enhanced photocatalytic performance under sunlight irradiation, *Phys. Chem. Chem. Phys.* 16 (2014) 23819–23828.
- [16] G. Zhang, G. Liu, L. Wang, J.T.S. Irvine, Inorganic perovskite photocatalysts for solar energy utilization, *Chem. Soc. Rev.* 45 (2016) 5951–5984.
- [17] E. Grabowska, M. Marchelek, T. Klimczuk, W. Lisowski, A. Zaleska-Medynska, TiO<sub>2</sub>/SrTiO<sub>3</sub> and SrTiO<sub>3</sub> microspheres decorated with Rh, Ru or Pt nanoparticles: highly UV-vis responsible photoactivity and mechanism, *J. Catal.* 350 (2017) 159–173.
- [18] T. Kanagaraj, S. Thiripuranthagan, Photocatalytic activities of novel SrTiO<sub>3</sub>–BiOBr heterojunction catalysts towards the degradation of reactive dyes, *Appl. Catal. B* 207 (2017) 218–232.
- [19] S. Jin, G. Dong, J. Luo, F. Ma, C. Wang, Improved photocatalytic NO removal activity of SrTiO<sub>3</sub> by using SrCO<sub>3</sub> as a new co-catalyst, *Appl. Catal. B* 227 (2018) 24–34.
- [20] R. Marschall, Semiconductor composites: strategies for enhancing charge carrier separation to improve photocatalytic activity, *Adv. Funct. Mater.* 24 (2014) 2421–2440.
- [21] H. Li, Y. Zhou, W. Tu, J. Ye, Z. Zou, State-of-the-art progress in diverse heterostructured photocatalysts toward promoting photocatalytic performance, *Adv. Funct. Mater.* 25 (2015) 998–1013.
- [22] L. Jiang, X. Yuan, Y. Pan, J. Liang, G. Zeng, Z. Wu, H. Wang, Doping of graphitic carbon nitride for photocatalysis: a review, *Appl. Catal. B* 217 (2017) 388–406.
- [23] S. Cao, J. Low, J. Yu, M. Jaroniec, Polymeric photocatalysts based on graphitic carbon nitride, *Adv. Mater.* 27 (2015) 2150–2176.
- [24] J. Low, C. Jiang, B. Cheng, S. Wageh, A.A. Al-Ghamdi, J. Yu, A review of direct Z-scheme photocatalysts, *Small Methods* 1 (2017) 1700080.
- [25] A. Hernández-Gordillo, V. Rodríguez-González, S. Oros-Ruiz, R. Gómez, Photodegradation of Indigo Carmine dye by CdS nanostructures under blue-light irradiation emitted by LEDs, *Catal. Today* 266 (2016) 27–35.
- [26] D. Sun, Y. Zhang, S. Yan, K. Sun, G. Wang, Y. Bu, G. Xie, Fabrication of excellent heterojunction assisting by interfaced oxygen vacancy to improve the separation capacity of photogenerated carriers, *Adv. Mater. Interfaces* 5 (2018) 1701325.
- [27] D. Zhong, W. Liu, P. Tan, A. Zhu, Y. Liu, X. Xiong, J. Pan, Insights into the synergy effect of anisotropic {001} and {230} facets of BaTiO<sub>3</sub> nanocubes sensitized with CdSe quantum dots for photocatalytic water reduction, *Appl. Catal. B* 227 (2018) 1–12.
- [28] Z. Wen, L. Zhu, L. Li, L. Sun, H. Cai, Z. Ye, A fluorine-mediated hydrothermal method to synthesize mesoporous rhombic ZnO nanorod arrays and their gas sensor application, *Dalton Trans.* 42 (2013) 15551–15554.
- [29] S. Kattel, P.J. Ramírez, J.G. Chen, J.A. Rodríguez, P. Liu, Active sites for CO<sub>2</sub> hydrogenation to methanol on Cu/ZnO catalysts, *Science* 355 (2017) 1296–1299.
- [30] Y. Zeng, Y. Wang, J. Chen, Y. Jiang, M. Kiani, B. Li, R. Wang, Fabrication of high-activity hybrid NiTiO<sub>3</sub>/g-C<sub>3</sub>N<sub>4</sub> heterostructured photocatalysts for water splitting to enhanced hydrogen production, *Ceram. Int.* 42 (2016) 12297–12305.
- [31] X. Chen, P. Tan, B. Zhou, H. Dong, J. Pan, X. Xiong, A green and facile strategy for preparation of novel and stable Cr-doped SrTiO<sub>3</sub>/g-C<sub>3</sub>N<sub>4</sub> hybrid nanocomposites with enhanced visible light photocatalytic activity, *J. Alloys. Compd.* 647 (2015) 456–462.
- [32] I. Papaailias, T. Giannakopoulou, N. Todorova, D. Demotikali, T. Vaimakis, C. Trapalis, Effect of processing temperature on structure and photocatalytic properties of g-C<sub>3</sub>N<sub>4</sub>, *Appl. Surf. Sci.* 358 (2015) 278–286.
- [33] K. Karthick, S.R. Ede, U. Nithiyannantham, S. Kundu, Low-temperature synthesis of SrTiO<sub>3</sub> nanoassemblies on DNA scaffolds and their applications in dye-sensitized solar cells and supercapacitors, *New J. Chem.* 41 (2017) 3473–3486.
- [34] R. Varadhaseshan, S.M. Sundar, C. Prema, On the preparation, structural and magnetic properties of ZnO:Co nanoparticles, *Eur. Phys. J. Appl. Phys.* 66 (2014) 10602.
- [35] J. Luan, M. Li, K. Ma, Y. Li, Z. Zou, Photocatalytic activity of novel Y<sub>2</sub>InSbO<sub>7</sub> and Y<sub>2</sub>GdSbO<sub>7</sub> nanocatalysts for degradation of environmental pollutant rhodamine B under visible light irradiation, *Chem. Eng. J.* 167 (2011) 162–171.
- [36] T.S. Natarajan, M. Thomas, K. Natarajan, H.C. Bajaj, R.J. Tayade, Study on UV-LED/TiO<sub>2</sub> process for degradation of Rhodamine B dye, *Chem. Eng. J.* 169 (2011) 126–134.
- [37] T. Liu, L. Wang, X. Lu, J. Fan, X. Cai, B. Gao, R. Miao, J. Wang, Y. Lv, Comparative study of the photocatalytic performance for the degradation of different dyes by ZnIn<sub>2</sub>S<sub>4</sub>: adsorption, active species, and pathways, *RSC Adv.* 7 (2017) 12292–12300.
- [38] M. Zaid, E. Chutet, S. Peulon, N. Bellakhal, B. Desmazières, M. Dachraoui, A. Chaussé, Spontaneous oxidative degradation of indigo carmine by thin films of birnessite electrodeposited onto SnO<sub>2</sub>, *Appl. Catal. B* 107 (2011) 42–51.
- [39] S. Kumar, S. Tonda, A. Baruah, B. Kumar, V. Shanker, Synthesis of novel and stable g-C<sub>3</sub>N<sub>4</sub>/N-doped SrTiO<sub>3</sub> hybrid nanocomposites with improved photocurrent and photocatalytic activity under visible light irradiation, *Dalton Trans.* 43 (2014) 16105–16114.
- [40] C.C. Wang, J.R. Li, X.L. Lv, Y.Q. Zhang, G. Guo, Photocatalytic organic pollutants degradation in metal-organic frameworks, *Energy Environ. Sci.* 7 (2014) 2831–2867.
- [41] L. Yu, X. Zhang, G. Li, Y. Cao, Y. Shao, D. Li, Highly efficient Bi<sub>2</sub>O<sub>3</sub>/CO<sub>3</sub>/BiOCl photocatalyst based on heterojunction with enhanced dye-sensitization under visible light, *Appl. Catal. B* 187 (2016) 301–309.
- [42] S. Kumar, A. Baruah, S. Tonda, B. Kumar, V. Shanker, B. Sreedhar, Cost-effective and eco-friendly synthesis of novel and stable N-doped ZnO/g-C<sub>3</sub>N<sub>4</sub> core-shell nanoplates with excellent visible-light responsive photocatalysis, *Nanoscale* 6 (2014) 4830–4832.